Buckling and postbuckling of etching-induced wiggling in a bilayer structure with intrinsic compressive stress

Dai Okumura [a,b,*], Junya Sugiura [c], Hiro Tanaka [a] and Yoji Shibutani [a,d]

[a] Department of Mechanical Engineering, Osaka University,
Yamadaoka, Suita, Osaka 565-0871, Japan
[b] Department of Mechanical Systems Engineering, Nagoya University,
Furo-cho, Chikusa-ku, Nagoya 464-8603, Japan
[c] Department of Computational Science and Engineering, Nagoya University,
Furo-cho, Chikusa-ku, Nagoya 464-8603, Japan
[d] Program in Nanotechnology, Vietnam Japan University,
My Dinh 1 Ward, Nam Tu Liem District, Ha Noi, Vietnam
* Corresponding author: okumura@mech.eng.osaka-u.ac.jp

Abstract:
In this study, we investigate buckling and postbuckling of etching-induced wiggling in a bilayer structure consisting of mask and masked layers. To show effects of explicit modeling of etching process, two mask–masked ridge models with and without etching (Models w/E and w/oE) are analyzed using finite element analysis. The etching process is explicitly introduced via step-by-step eigenvalue buckling analysis. Although Model w/oE predicts a constant value of the critical wavelength of wiggling regardless of the change in ridge width, Model w/E predicts a shorter wavelength depending on the decrease in ridge width and the increase in intrinsic compressive stress in the mask layer. In postbuckling analysis, Model w/oE predicts a monotonic increase in the wiggling amplitude with the constant wavelength, whereas Model w/E predicts saturation of the wiggling amplitude owing to the decreasing wavelength. In the explicit modeling of etching process, the wiggling behavior shows completely opposite tendencies. Dimensional analysis is performed to obtain empirical equations, which are compared with an experiment.

Keywords: Wiggling, Etching, Bilayer structure, Buckling, Postbuckling, Finite element analysis

1. Introduction

The etching process is considered an irreplaceable process in the fabrication of semiconductor devices [1–5], and is applied to bilayer structures consisting of mask and masked (dielectric) layers. The unmasked regions of the masked layer are selectively removed by dry plasma etching to produce mask–masked ridges (Fig.1). An intrinsic compressive stress acts inside the mask layer, the extent of which is mainly determined by the combination of the mask and masked materials. To create highly integrated, dense, high-performance semiconductor circuits, the width of the resulting ridges has steadily decreased each year and is forecast to reach sub-10 nm levels by 2025 [5]. The mask–masked ridges are expected to have a higher height-to-width aspect ratio, leading to structural instability because the lower stiffness of the ridges does not prevent buckling from releasing the elastic strain energy of the intrinsic compressive stress. That is, wiggling instability occurs, with a lateral undulation emerging in the longitudinal direction of the mask–masked ridges [1,5,6].

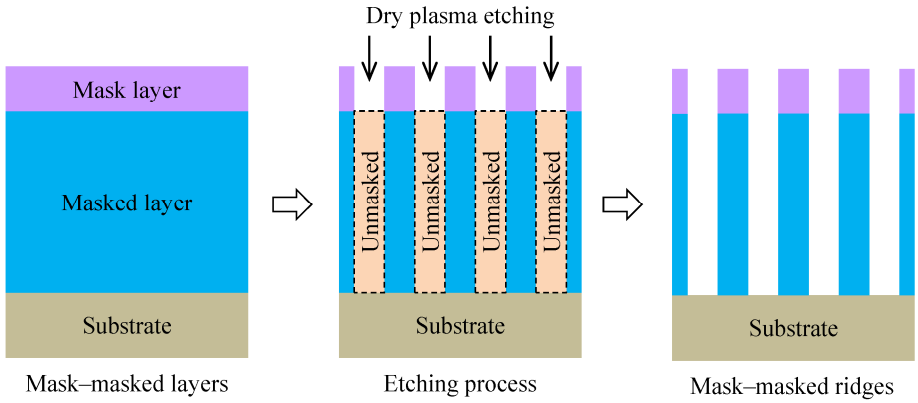

Fig.1 Schematic illustrations of the formation of mask–masked ridges by plasma etching of a bilayer structure consisting of mask and masked layers.

A similar wiggling instability has been observed in gel ridges consisting of a single material constrained on a substrate [7–11]. In this specific case, the increase in swelling of solvent molecules induces an increase in the compressive stress in the gel ridges. Swelling-induced wiggling can be investigated by analyzing a monolayer ridge using a simple approach based on Föppl–von Kármán (FVK) plate theory. More detailed finite element analysis can also be performed using the inhomogeneous field theories for polymeric gels [12–17]. However, for the analysis of a bilayer structure with mask and

masked layers, the mask layer includes the intrinsic compressive stress before etching, and the etching process causes wiggling instability, i.e., etching-induced wiggling occurs in mask–masked ridges.

The mask–masked ridge was first analyzed using the finite element method (FEM) [1] and was then evaluated using a bilayer model of the FVK plate theory [5]. Darnon et al. [1] performed eigenvalue buckling analysis of mask–masked ridges with final dimensions after etching and estimated the critical compressive stress in the mask layer; i.e., for simplicity, the etching process was not explicitly modeled in the analysis. They demonstrated the effects of the ridge width, etched height, and Young's modulus of the masked layer and intrinsic stress in the mask layer on the critical load of the wiggling instability. Although their investigation was performed without the inclusion of an etching process, Tanaka et al. [5] introduced the etching effect into their analytical framework based on FVK plate theory. In their paper, a linear system of dimensionless equations was successfully derived to investigate the effect of geometrical and material parameters on the critical load and wavenumber of the wiggling instability. The intrinsic compressive stress and etched height of the masked layer were used to define a dimensionless load, Λ, and, furthermore, the ratio of the mask height to the etched height of the masked layer was defined as a measure of the etching process, κ. They plotted a normalized stability diagram as a function of Λ and κ, and demonstrated that most available estimates agreed well with their experiments [5].

Generally speaking, the eigenvalue buckling analysis with the final ridge profile [1] may be sufficient to detect whether wiggling instability occurs because buckling occurs during etching process if the critical compressive stress is larger than the actual intrinsic stress in the mask layer. However, when temporal dimensions during etching are estimated as the critical dimensions [5], which differ from the final dimensions, this difference must have substantial effects on the critical wavelength of wiggling, resulting in a change of the amplitude of wiggling after buckling. The aforementioned aspects were not considered in the previous study [5]. In addition, their modeling based on the FVK plate theory was restricted to analyzing buckling points with very thin ridge structure. It would be meaningful to consider how the etching process is implemented in

eigenvalue buckling and postbuckling FEM analyses. That is because if the explicit introduction of the etching process results in considerable differences in the tendencies of the critical wavelength and amplitude of wiggling, this knowledge would be beneficial in improving the fabrication processes of mask–masked ridges. Thus, it is worthwhile to investigate and understand the effects of the etching process on the critical wavelength of wiggling and on the evolution of the wiggling amplitude.

In this study, we investigate buckling and postbuckling of etching-induced wiggling in a bilayer structure consisting of mask and masked layers. In Section 2, to analyze effects of explicit modeling of etching process, two mask–masked ridge models with and without etching (Models w/E and w/oE) are developed for eigenvalue buckling and postbuckling FEM analyses. The etching process is explicitly introduced via step-by-step eigenvalue buckling analysis. Sections 3 and 4 present the results of eigenvalue buckling and postbuckling analyses, respectively. It is found that in the explicit modeling of etching process, the wiggling behavior shows completely opposite tendencies. In Section 5, dimensional analysis is performed to obtain empirical equations, which is compared with an experiment. The possibility of the occurrence of a second bifurcation after buckling is also discussed. Finally, concluding remarks are provided in Section 6.

2. Etching process in finite element modeling

2.1. Models w/E and w/oE

Fig.2 presents schematic illustrations of the two finite element models with and without the etching process analyzed in the present study. Here, b and L are the width and length of the mask–masked ridge, respectively, and h and h_{m} are the height of the masked and mask layers, respectively. Fig.2a shows the final dimensions after etching, used as the model without the etching process (i.e., Model w/oE). Fig.2b and 2c show the initial dimensions before etching and the temporal dimensions during etching, respectively, which are used as the model with the etching process (i.e., Model w/E). Etching is the process used to selectively remove the unmasked regions in the masked layer on the lateral sides of the final dimensions. Model w/E has the ability of reproducing the etching process (Fig.2b,c). Etching of the unmasked regions is assumed to progress uniformly from the top face (y=h) to the bottom face (y=0) (Fig.1). In the

finite element analysis, instead of eliminating the finite elements removed by etching, a sufficiently small Young's modulus is given to the etched finite elements to introduce the equivalent effect of eliminating them. The etched height, Δh ($0 \le \Delta h \le h$), is defined as the distance etched from the top face (Fig.2c). The Young's modulus of the unmasked regions, E_{um}, changes from the value of the original material to a sufficiently small value as a function of the etched height; that is,

$$E_{\mathrm{um}} = \begin{cases} E & (0 \le y \le h - \Delta h) \\ cE & (h - \Delta h < y \le h) \end{cases}, \tag{1}$$

where E is Young's modulus of the masked layer and c=10^{-6} is used as a sufficiently small coefficient in the present study.

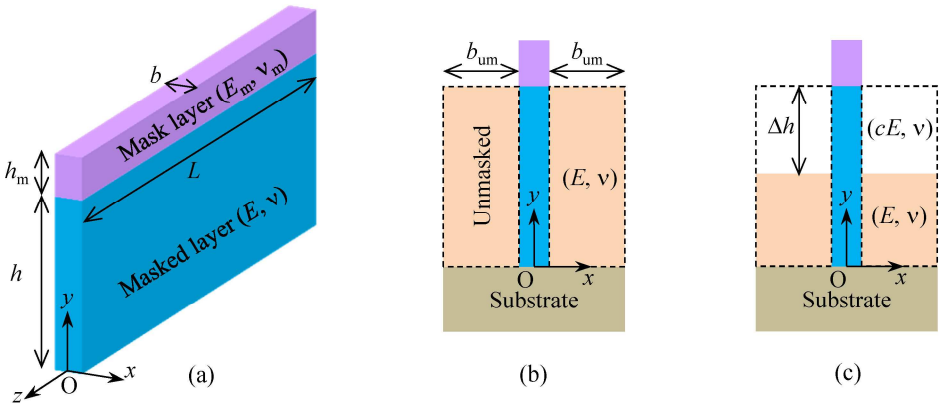

Fig.2 Two finite element models with and without etching process: (a) finial dimensions after etching (Model w/oE), (b) initial dimensions before etching (Model w/E), and (c) temporal dimensions during etching (Model w/E).

2.2. Materials and dimensions

In experimental measurements of wiggling of the corresponding bilayer structure [5], the mask and masked materials were hydrogenated amorphous silicon and hydrogenated amorphous carbon, respectively. The Young's modulus and Poisson's ratio were E_{m}=122 GPa and ν_{m}=0.3 for the mask material and E=12.8 GPa and ν=0.3 for the masked material; these values are applied in the present analysis. Although Tanaka et al. [5] experimented with several samples of different dimensions (h=85−265 nm, h_{m}=24−35 nm and b=21−27 nm), in the present study, h=258 nm and h_{m}=26 nm are used as representative values, and b is assumed to fall in the range of b=10−35 nm. The intrinsic

compressive stress in the mask layer is approximately σ=1 GPa in the experiments. This value is used as the representative value in the present study. But, to investigate the effect, the value of σ is also assumed to fall in the range of σ=0−1.2 GPa. The ridge width and intrinsic compressive stress, b and σ, are parameterized to investigate the effects on the wiggling behavior of the mask–masked ridges.

It is noted that L=5000 nm and b_{um}=50 nm are used but are not actual dimensions. The actual dimension of L is considerably longer than 5000 nm [5]. The experimentally observed wavelengths are smaller than 1000 nm (Section 5.3). The value of L=5000 nm is sufficient to capture the expected wavelengths (Appendix A). The value of b_{um}=50 nm is just used as a sufficiently thick value to reproduce the constraints of the unmasked regions.

2.3. Finite element discretization

The finite element software Abaqus [18] is used for the eigenvalue buckling and post-buckling analyses. The problem to be solved is analyzed as a three-dimensional problem using the 8-node linear brick element with reduced integration, the element type C3D8R. This element type is used to obtain fine finite element solutions. The 8-node linear brick incompatible element, C3D8I, and the 20-node quadratic brick element, C3D20, can also be available but the 8-node linear brick element, C3D8, should not be used to cause an unphysically stiff response of deformation, i.e., locking phenomena [18–20]. The individual lengths of L, h, h_m, b, and b_{um} are equally divided by 257, 81, 9, 9, and 5 nodes, respectively. These values were determined by trial and error analysis to obtain sufficiently fine finite element solutions. Although the shapes of the mask–masked ridge are simple (Fig.2), Models w/oE and w/E have 205857 and 372393 nodes, and 180224 and 344064 elements, respectively. In addition, if 370 nm is considered as a shorter wavelength of wiggling (Section 3), this wavelength consists of approximately 19 elements. This mesh resolution is fine for eigenvalue buckling and postbuckling analyses because of the element type C3D8R [18,19].

For both Models w/oE and w/E, the displacements of the bottom face (y=0) are fixed because of the constraint of a rigid substrate, whereas the other displacements are

only constrained along the z-direction on the two ends of the ridges (z=0 and $-L$). This constraint allows the wavelength of wiggling to be discretized depending on the length L in the eigenvalue buckling analysis (Appendix A).

Prebuckling and postbuckling analyses of Models w/oE and w/E are performed as follows. Since Model w/oE consists of the final dimensions after etching, the etched height of the masked layer, Δh, is fixed at the value of the final dimension, i.e, $\Delta h = h$. This model is analyzed by increasing the value of the intrinsic compressive stress in the mask layer, $\Delta\sigma$, from 0. In contrast, since Model w/E considers the etching process, $\Delta\sigma$ is first increased from 0 to σ, and Δh is then increased from 0 to h. In the present study, $\Delta\sigma$ is given using the isotropic thermal expansion, while Δh is controlled using a dimensionless field variable (Appendix B). Additionally, automatic time incrementation is used in the Abaqus analysis. If a solution for an increment fails to converge, the incremental size is decreased until a converged solution is found. In the present analysis, when a converged solution is not found even for extremely small increments, the incremental analysis is regarded as no convergence.

2.4. Step-by-step eigenvalue buckling and postbuckling analyses

Eigenvalue buckling analysis (the BUCKLE option in Abaqus) is performed to investigate the critical points of wiggling, $\Delta\sigma_c$ for Model w/oE and Δh_c for Model w/E. From the corresponding buckling mode, the critical wavelength of wiggling, λ_c, is estimated (Appendix A).

The eigenvalue problem is analyzed by solving the following finite element equations [18,21],

$$\left\{\mathbf{K}_0(P) + \kappa_i \mathbf{K}_\Delta(P,Q)\right\}\boldsymbol{\phi}_i = \mathbf{0}, \tag{2}$$

where $\mathbf{K}_0(P)$ is the stiffness matrix at the base state, which includes the effects of preloads P; $\mathbf{K}_\Delta(P,Q)$ is the differential initial stress and load stiffness matrix resulting from the incremental loading pattern Q; κ_i are the eigenvalues; and $\boldsymbol{\phi}_i$ are the corresponding buckling modes, where i indicates the i-th buckling mode. They are normalized such that the maximum displacement component is 1.

When $\mathrm{Det}\left\{\mathbf{K}_0(P)+\kappa_i\mathbf{K}_\Delta(P,Q)\right\}=0$ is checked by changing κ_i, the critical buckling loads are expressed by $P+\kappa_i Q$. If P is absent, they are expressed by $\kappa_i Q$. If the adjusted magnitude of P allows the resulting base state to be at a buckling point, the critical buckling load is expressed by P. At least one of κ_i is zero in Eq.(2), independent of the selection of Q. When $\kappa_1=0$, Eq.(2) is simply reduced to

$$\mathbf{K}_0(P)\boldsymbol{\phi}_1=\mathbf{0}, \tag{3}$$

Eq.(3) results in $\mathrm{Det}\,\mathbf{K}_0(P)=0$, which is the equation used to find the typical bifurcation point without Q [22–24].

When Model w/oE is analyzed using Eq.(2), P is not needed and the buckling loads $\Delta\sigma_c$ are estimated by $\Delta\sigma_c=\kappa_1\Delta\sigma_{unit}$, i.e., $\Delta\sigma_{unit}=1$ MPa is used as Q. Here, $\Delta\sigma_c$ is the buckling compressive stress in the mask layer, which is compared with the intrinsic compressive stress σ. This approach is identical to that of Darnon et al. [1]. In contrast, when Model w/E is analyzed using Eq.(2), $\Delta\sigma=\sigma$ must be given as P beforehand, and Δh_c is then expected to be given as $\Delta h_c=\kappa_1\Delta h_{unit}$. However, in this case, Δh_{unit} is not available as Q because Eq.(2) is based on linear perturbation analysis, and the stiffness change in the etched layers (Eq.(1)) is not considered in Abaqus [18]. For this reason, the step-by-step increases of Δh must also be included in P. Moreover, the further compressive stress, $\Delta\sigma_{add}$, from $\Delta\sigma=\sigma$ is used as $\Delta\sigma_{add}=\kappa_1\Delta\sigma_{unit}$. In this case, $\Delta\sigma_{add}$ has no physical meanings and acts as a dummy loading parameter [25]. When eigenvalue buckling analysis is performed using individual base states including the step-by-step evolution of Δh, the lowest eigenvalue, κ_1, decreases to 0 with etching progress. The base state with $\kappa_1=0$ (in fact, $\kappa_1\approx0$) is regarded as the buckling point described by Eq.(3). The value of Δh at this base state is estimated as Δh_c. The effect of the dummy loading parameter $\Delta\sigma_{add}$ is canceled by searching for the critical point expressed by Eq.(3). It is noted that Model w/E requires additional computational costs caused by step-by-step eigenvalue buckling analyses; however, the costs allow Model w/E to be analyzed with explicit modeling of the etching process and allow the critical etching height, Δh_c, to be estimated via the step-by-step analyses.

To analyze the evolution of the wiggling amplitude after buckling in postbuckling analysis, the dominant buckling mode is introduced as a geometric imperfection (the IMPERFECTION option in Abaqus). The perturbation, $\Delta\phi$, introduced as initial geometrical imperfections, is expressed as

$$\Delta\phi = db\phi_1, \tag{4}$$

where b is the width of the mask–masked ridge and d is the scale factor. In the present study, d =0.001 is used as a standard value; however, for b=10 nm, d=0.01 is used because d=0.001 failed to trace the bifurcated path in the postbuckling analysis.

3. Eigenvalue buckling analysis

Tanaka et al. [5] derived a normalized stability diagram of wiggling instability using a dimensionless load, which consisted of dimensional parameters; the intrinsic compressive stress, σ; and the width and height of the mask–masked ridge, b and $h+h_m$, respectively. They did not focus on the following points in their paper; (1) the critical compressive stress, $\Delta\sigma_c$, for Model w/oE, (2) the critical etched height, Δh_c, for Model w/E, and (3) the resulting critical wavelength, λ_c. But, these dimensional values are calculated by specifically introducing the dimensional parameters via the stability diagram. In this section, to investigate the critical points of Models w/oE and w/E, in addition to eigenvalue buckling analysis in the FEM (Section 2), the bilayer model based on the FVK plate theory [5] is also analyzed. The results are compared with a discussion of the effects of the etching process on the critical point. In all the figures in this section, the individual results obtained from two different approaches are simply tagged as FEM and FVK, respectively.

Fig.3 presents the wiggling wavelength results measured from the buckling modes, which are solved using the eigenvalue buckling analysis of Model w/oE. Here, σ=1 GPa is used as the representative value. Individual buckling modes have wavelengths discretized by the positive integer n, i.e., $\lambda=2L/n$ (Appendix A). For b=20 nm, the 1st buckling mode appears at $\Delta\sigma_c/\sigma$=0.423 with n=8, whereas the 2nd and 3rd buckling modes occur at $\Delta\sigma/\sigma$=0.428 and 0.432 with n=7 and 9, respectively. The FEM results indicate that the critical wavelength is approximately 1250 nm in the range of 1111−

1429 nm.

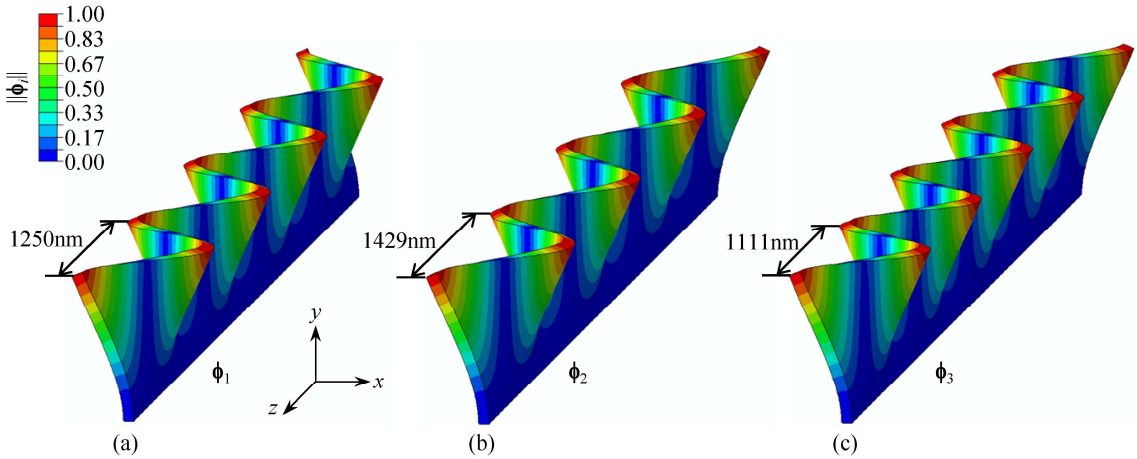

Fig.3 Relations of wiggling wavelengths, λ, and buckling modes, ϕ_i, for b=20 nm in Model w/oE; (a) 1st buckling mode ϕ_1 ($\Delta\sigma_c/\sigma$ =0.423, n=8, λ_c=1250 nm), (b) 2nd buckling mode ϕ_2 ($\Delta\sigma/\sigma$ =0.428, n=7, λ=1429 nm) and (c) 3rd buckling mode ϕ_3 ($\Delta\sigma/\sigma$ =0.432, n=9, λ=1111 nm).

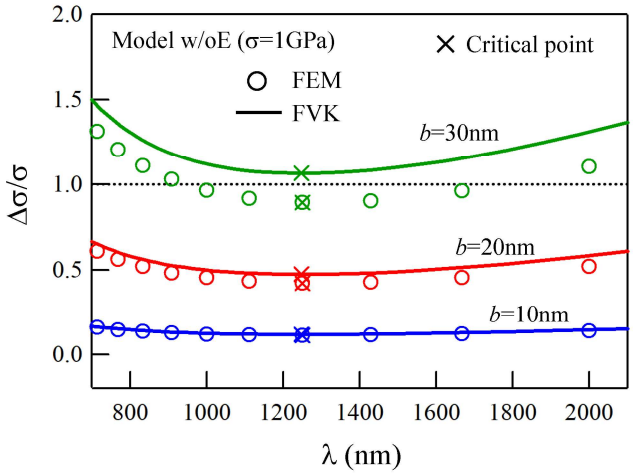

Fig.4 Compressive stress, $\Delta\sigma/\sigma$, as a function of wavelength, λ, for b=10, 20, and 30 nm for Model w/oE.

Fig.4 shows the compressive stress, $\Delta\sigma/\sigma$, as a function of the wavelength, λ. Comparison of the FEM and FVK results indicates that both approaches successfully estimate the same dependences of λ and b on $\Delta\sigma/\sigma$. As b decreases from 30 to 10 nm, the difference between the FEM and FVK results is reduced, especially for b=10 nm, for which the profiles are almost identical. This tendency indicates that the FEM and FVK results reciprocally verify each other as a thin plate is assumed in the FVK plate theory. As a result, with increasing thickness of the plate, i.e., b, the FVK approach gradually

overestimates the compressive stress compared with the FEM approach. However, the FVK model predicts the critical wavelength $\lambda_c \approx 1248$ nm independent of b with $\Delta\sigma_c/\sigma = 0.118$, 0.474 and 1.066 for b=10, 20 and 30 nm, respectively. Similarly, the FEM model also predicts λ_c=1250 nm as the 1st buckling mode regardless of b with $\Delta\sigma_c/\sigma$=0.113, 0.423, and 0.895 for b=10, 20, and 30 nm, respectively. Model w/oE is found to predict the critical wavelength that is independent of b with the constant value of $\lambda_c \approx 1250$ nm.

Since σ=1 GPa is referred to as the representative value [5], the FEM results for Model w/oE predict $\Delta\sigma_c/\sigma < 1$ for b=10, 20, and 30 nm (Fig.4), such that wiggling instability is expected to occur during the etching process. Figs.5 and 6 show that Model w/E, i.e., introduction of the etching process, causes completely different wiggling responses than Model w/oE. As observed in Fig.5b, the critical wavelength, λ_c, decreases dramatically from 1250 to 370 nm when b decreases from 32 to 10 nm. Fig.6 shows the 1st buckling modes at the critical etched height, $\Delta h_c/h$, which is captured by step-by-step eigenvalue buckling analysis using Eqs. (2) and (3). In these figures, the specific finite elements, which are assumed to be eliminated by etching (Eq.(1)), are invisible. Fig.5a shows the effect of b on the critical etched height, $\Delta h_c/h$. As expected from the results of Model w/oE, as b decreases with the intrinsic compressive stress σ=1 GPa, etching-induced buckling occurs in an earlier stage of the etching process because the stiffness of the mask–masked ridge decreases. The dominant wiggling wavelength decreases with reduced etched height. This finding may be qualitatively understood by considering the wiggling instability of a monolayer problem because the results obey a scaling relation [7,8]; however, in the present study, the value of h_m=26 nm is fixed. Thus, the mask–masked ridge structure, i.e., the bilayer structure, does not simply obey the scaling relation of the monolayer structure. To discuss this problem, dimensional analysis will be performed in Section 5.1.

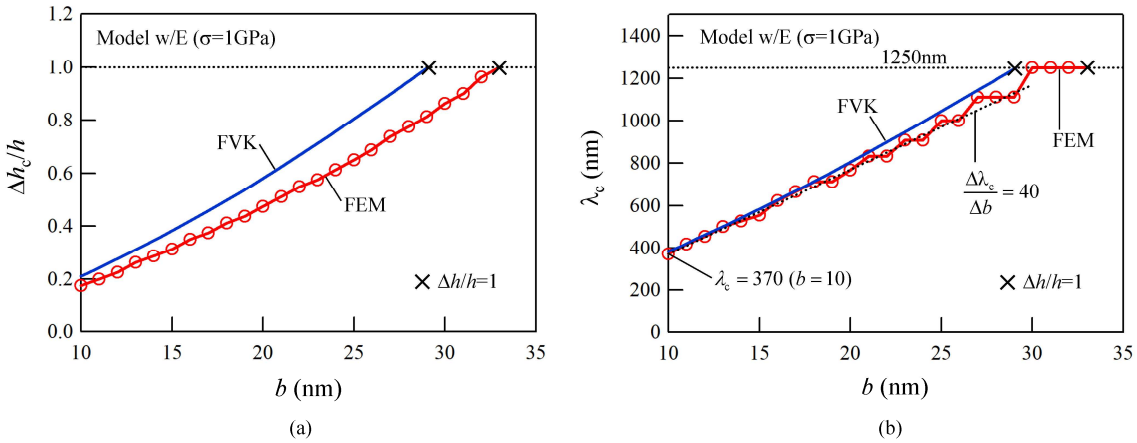

Fig.5 Effects of b on critical buckling point predicted in Model w/E: (a) critical etching depth, $\Delta h_c/h$, and (b) critical wavelength, λ_c.

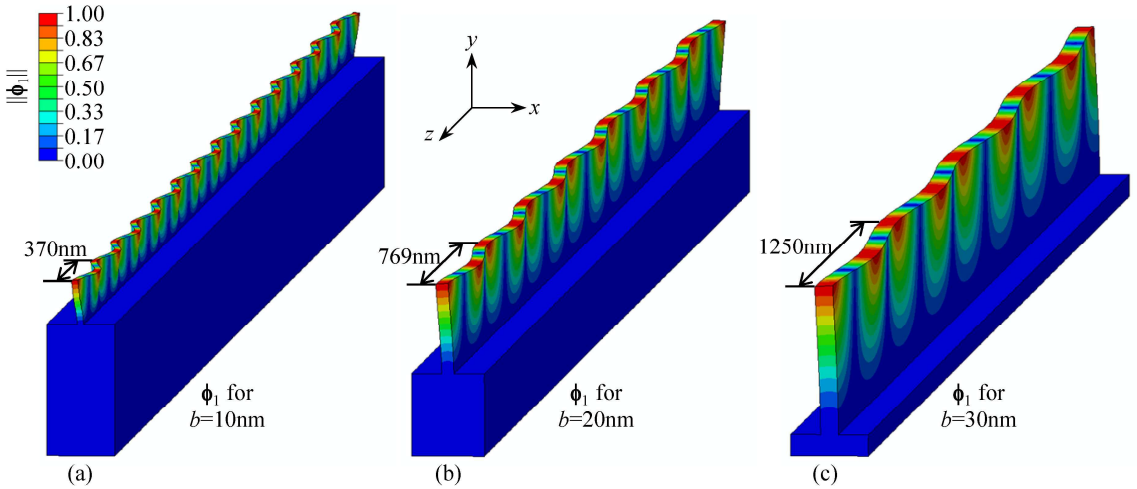

Fig.6 1st buckling mode, ϕ_1, in Model w/E for (a) b=10 nm ($\Delta h_c/h$=0.175, n=13.5, λ_c=370 nm), (b) b=20 nm ($\Delta h_c/h$=0.475, n=6.5, λ_c=769 nm), and (c) b=30 nm ($\Delta h_c/h$=0.863, n=4, λ_c=1250 nm).

Upon comparing the FEM and FVK approaches in Figs.5 and 6, the tendencies are observed to be the same as those obtained using Model w/oE. The FVK approach gradually overestimates the critical etched height, $\Delta h_c/h$, as b increases from 10 nm. No wiggling instability occurs for b>29 nm for the FVK approach, while b>32 nm for the FEM approach (Fig.5a). However, the critical wavelengths predicted by the FVK model agree well with those by the FEM model. The employment of the FVK approach [5] causes the overestimation of the critical value of loading parameters, i.e., $\Delta\sigma_c/\sigma$ for Model w/oE and $\Delta h_c/h$ for Model w/E, when the value of b cannot be regarded as a thin plate. In contrast, the critical wavelength is independent of this overestimation and is in

good agreement with that predicted by FEM. It is noted that in Fig.5b, the FEM model predicts a stepwise change in the critical wavelength near b=22−32 nm. This secondary effect is caused by the relation of L and λ (Appendix A), and is similar to the buckling response of a flat corona of a gel [7].

4. Postbuckling analysis

When postbuckling analysis is performed in finite element analysis (i.e., FEM) using Models w/oE and w/E, the evolution of the wiggling amplitude must reflect a monotonic increase. This amplitude evolution is analyzed by increasing $\Delta\sigma/\sigma$ from 0 to 1 for Model w/oE (Fig.7), and increasing $\Delta h/h$ from 0 to 1 for Model w/E (Fig.8). Here, the maximum amplitude, A, is defined as the maximum displacement in the x-direction at the center line parallel to the top face ($y=h_m+h$) of the mask–masked ridge in z-direction. As expected, the change in A shows a monotonic increase regardless of the use of Model w/oE or w/E (Figs.7 and 8); however, the difference in the critical wavelengths (for b=20 nm, 1250 nm for Model w/oE and 769 nm for Model w/E) results directly in the difference of A. The introduction of the etching process dramatically decreases not only the critical wavelength λ_c (Fig.5) but also the resulting maximum amplitude A (Fig.8).

Fig.9 shows the amplitude evolution as a function of $\Delta\sigma/\sigma$ for Model w/oE (Fig.9a) and as a function of $\Delta h/h$ for Model w/E (Fig.9b). Although Models w/oE and w/E are used to estimate the amplitude evolution with the representative value of σ=1 GPa, Model w/E is also used for changing σ with a constant value of b=10 nm (Fig.9c). The results of eigenvalue buckling analysis are shown in Appendix C. First, for Model w/oE, the critical wavelength is λ_c=1250 nm independent of b (Fig.4), and as b decreases, wiggling instability begins at an earlier stage of increasing $\Delta\sigma/\sigma$. Thus, the final amplitude increases as b decreases (Fig.9a). In contrast, surprisingly, opposite responses are predicted by Model w/E. In other words, the final amplitude decreases as b decreases except for b=30 nm (Fig.9b). This finding is observed because the decrease in b allows buckling to occur at an earlier stage of etching (Fig.5a) and allows the critical wavelength to become shorter (Fig.5b). As shown in Fig.9b, although the evolution of the amplitude starts directly after reaching the critical etched height, this evolution does not maintain a steady increase and is saturated. Etched layers after this saturation makes almost no contribution to the amplitude evolution. It is understood that the maximum

energy release due to buckling requires a long wavelength, as predicted based on the final dimensions (Model w/oE). However, in fact, etching-induced buckling occurring at the temporal dimensions (Model w/E) decreases the critical wavelength, which does not allow the maximum energy release, leading to a smaller energy release with a shorter wavelength.

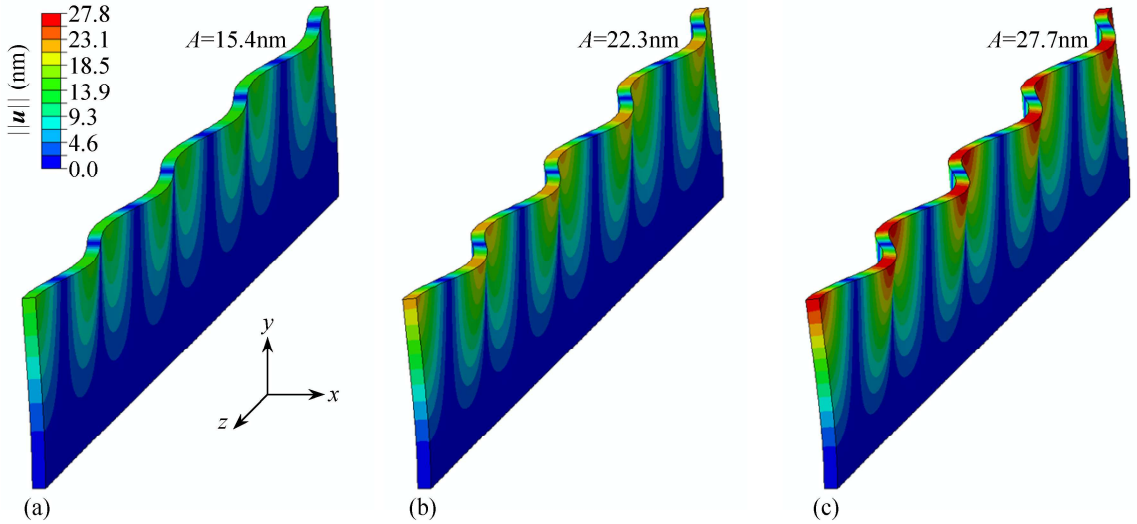

Fig.7 Snapshots of amplitude evolution for Model w/oE in postbuckling analysis (b=20 nm, $\Delta\sigma_c/\sigma$=0.423, λ_c=1250 nm) for (a) $\Delta\sigma/\sigma$=0.6, (b) $\Delta\sigma/\sigma$=0.8, and (c) $\Delta\sigma/\sigma$=1.

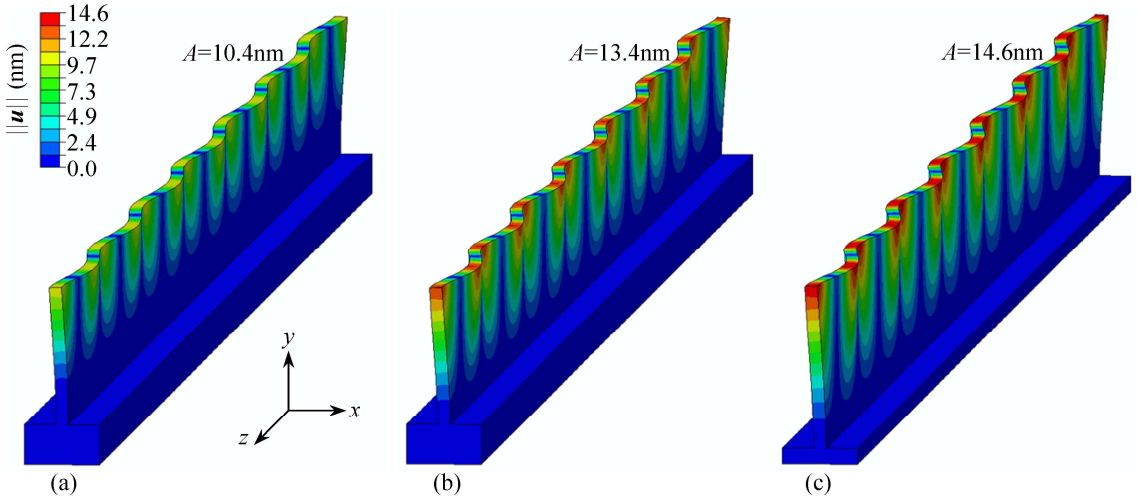

Fig.8 Snapshots of amplitude evolution for Model w/E in postbuckling analysis (b=20 nm, $\Delta h_c/h$=0.475, λ_c=769 nm) for (a) $\Delta h/h$=0.6, (b) $\Delta h/h$=0.75, and (c) $\Delta h/h$=0.9.

In this case, to obtain an additional energy release, a second bifurcation with a longer wavelength may occur after buckling, especially after the saturation of the wiggling amplitude. In Fig.9b,c, the maker △ indicates failure of the incremental

analysis to obtain a converged solution (Section 2.3). As will be discussed in Section 5.2, this problem can be related to the second bifurcation after buckling. To obtain the final amplitude at $\Delta h/h$=1, a different version of Model w/oE with L=0.5λ_c was analyzed. The results are plotted using the maker ○ in Fig.9b,c. The amplitude at the maker △ is found to have no difference to that at the maker ○.

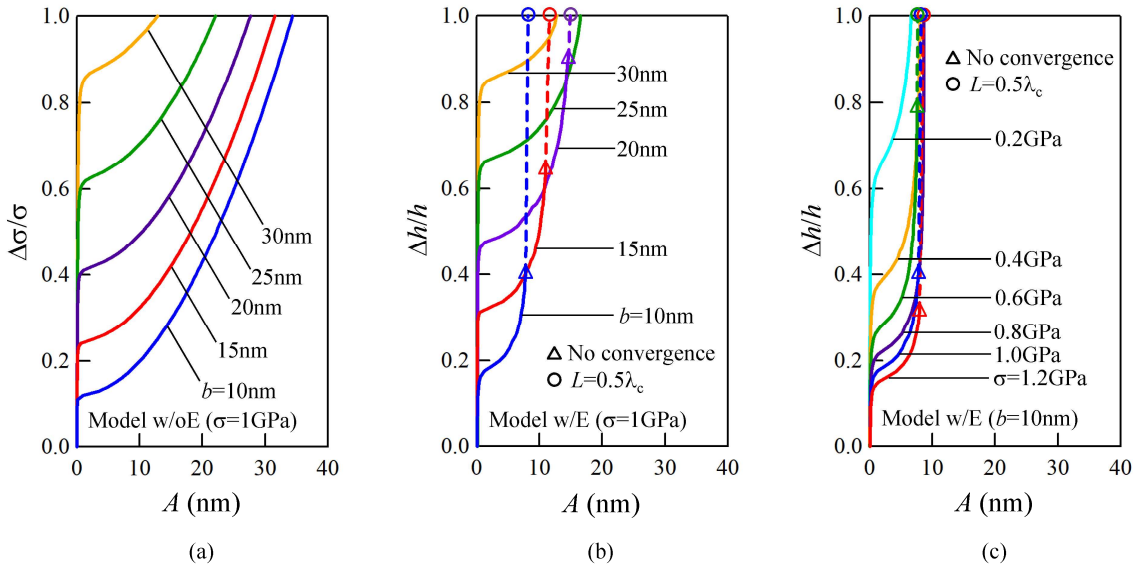

Fig.9 Amplitude evolution as a function of (a) $\Delta\sigma/\sigma$ for Model w/oE (σ=1 GPa) and $\Delta h/h$ for Model w/E with (b) σ=1 GPa and (c) b=10 nm.

Fig.9b focuses on the responses of Model w/E, demonstrating that the values of the saturated amplitudes clearly depend on the values of b with the constant value of σ=1 GPa. Fig.9c shows that these values are almost independent of the change in σ for the constant value of b=10 nm. In Fig.10a and 10b, the final amplitudes after etching, A_f, are plotted as a function of b and σ, respectively. Model w/oE has the long wavelength of 1250 nm such that both the decrease of b and the increase of σ result in a steady increase of the amplitude. In contrast, owing to the introduction of the etching process, Model w/E has a shorter wavelength depending on both the decrease of b and increase of σ (Figs.5 and C). Fig.10a shows that the decrease in b plays a characteristic role in causing an approximately linear decrease in A_f although A_f first increases with b decreasing as in Model w/oE. Fig.10b shows the change in σ hardly contributes to the change in A_f. In the next section (Section 5.1), based on the aforementioned findings and relations, empirical equations will be obtained from dimensional analysis.

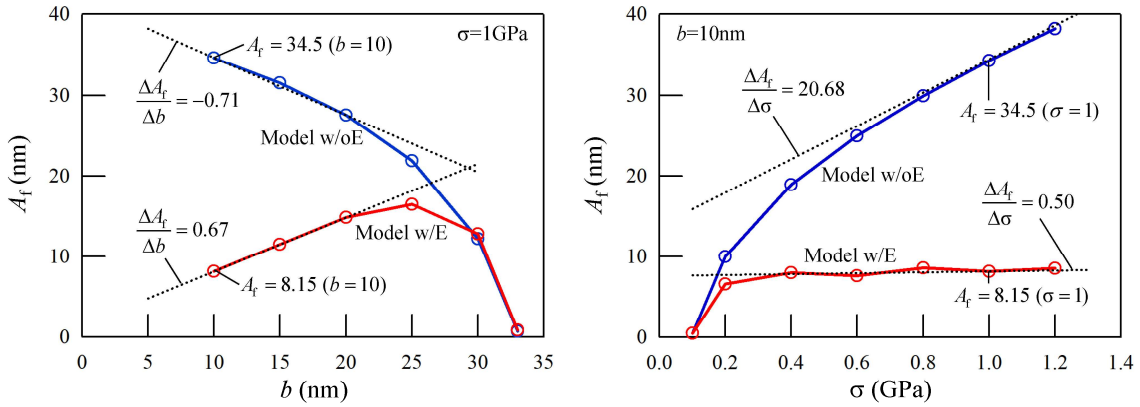

Fig.10 Final amplitudes at $\Delta\sigma/\sigma$=1 for Model w/oE and $\Delta h/h$=1 for Model w/E as a function of (a) b with σ=1 GPa and (b) σ with b=10 nm.

5. Discussions

5.1. Empirical equations obtained from dimensional analysis

Sections 3 and 4 demonstrated that the introduction of the etching process, i.e., the use of Model w/E instead of Model w/oE, resulted in the prediction of complex responses in etching-induced wiggling of the mask–masked ridge. Here, dimensional analysis is performed to obtain empirical equations for the critical wavelength, λ_c, and the final amplitude at the final dimensions, A_f. The dependence of λ_c and A_f on physical variables is discussed.

According to the Buckingham π theorem [26], the problem to be solved has two physical dimensions, distance dimension and pressure dimension (Section 2). Physical variables are h_m, b, Δh, E, E_m and $\Delta\sigma$. Further, λ and A are added to consider λ_c and A_f. Since the present study considered h_m=26 nm and E_m=122 GPa as the constant values, it is natural to normalize distance and pressure dimensions using h_m and E_m, respectively, i.e., dimensionless parameters are b/h_m, $\Delta h/h_m$, E/E_m, $\Delta\sigma/E_m$, λ/h_m and A/h_m. Thus if these dimensionless parameters are used to obtain empirical equations for λ_c and A_f, the responses without h_m=26 nm and E_m=122 GPa can also be estimated via scaling relations.

To reduce the dimensionless parameters, when E/E_m=12.8/122=0.105 is fixed (Section 2.2), λ/h_m is assumed to have a function of b/h_m, $\Delta h/h_m$ and $\Delta\sigma/E_m$. The critical wavelength, λ_c, is predicted when Δh=h=258 nm and $\Delta\sigma$=$\Delta\sigma_c$ for Model w/oE and

when $\Delta h=\Delta h_c$ and $\Delta\sigma=\sigma$ for Model w/E, respectively. For Model w/oE, λ_c/h_m is a function of b/h_m with $h/h_m=258/26=9.923$, whereas for Model w/E, λ_c/h_m is a function of b/h_m and σ/E_m, that is,

$$\frac{\lambda_c}{h_m}=\begin{cases} f\left(\dfrac{b}{h_m}\right), & \text{for Model w/oE} \\ f\left(\dfrac{b}{h_m},\dfrac{\sigma}{E_m}\right), & \text{for Model w/E} \end{cases} . \tag{5}$$

In the same manner, A/h_m is assumed to have a function of b/h_m, $\Delta h/h_m$, $\Delta\sigma/E_m$ and λ/h_m. When $h/h_m=9.923$, $\Delta\sigma=\sigma$ and $\lambda=\lambda_c$, the final amplitude at the final dimensions, A_f, is predicted, that is,

$$\frac{A_f}{h_m}=g\left(\frac{b}{h_m},\frac{\sigma}{E_m}\right), \quad \text{for Models w/oE and w/E} . \tag{6}$$

In Sections 3 and 4, the parametric analysis was performed to investigate the dependence of λ_c and A_f on b and σ (see Figs.4, 5, 10 and C). This investigation allows us to obtain empirical equations from Eqs.(5) and (6).

First of all, for Model w/oE, λ_c/h_m is a function of b/h_m (Eq.(5)). Fig.4 indicates that λ_c is the constant value of $\lambda_c=1250$ nm and is independent of b. This means that if $E/E_m=0.105$ and $h/h_m=9.923$, Eq.(5) yields

$$\frac{\lambda_c}{h_m}=\frac{1250}{26}=48.08, \qquad \text{for Model w/oE} , \tag{7}$$

which is rewritten as $\lambda_c=48.08h_m=4.845h$, resulting in $\lambda_c=4.401(h_m+h)$. Mora and Boudaoud [7] derived $\lambda_c=3.256l$ for a monolayer ridge, where l is the height of the ridge, i.e., $l=h_m+h$ in the present study. The comparison of these relations implies that the bilayer ridge structure can have a similar scaling relation to the monolayer ridge structure. The difference between 4.401 for the bilayer structure and 3.256 for the monolayer structure is interpreted as a bilayer effect. The bilayer structure plays a role in increasing the critical wavelength. In the present study, the coefficient of 4.401 was obtained under $E/E_m=0.105$ and $h/h_m=9.923$. If $h/h_m\to 0$, the coefficient of 3.256 is

expected because of the monolayer ridge. The coefficient is found to depend on the combination of E/E_m and h/h_m.

For Model w/E, λ_c/h_m is a function of b/h_m and σ/E_m (Eq.(5)). The responses depicted in Fig.5b and Fig.Cb enable Eq.(5) to be approximately expressed by the following simple form

$$\frac{\lambda_c}{h_m} \approx \alpha_1\left(\frac{b}{h_m}\right)+\alpha_2\left(\frac{\sigma}{E_m}\right)+\alpha_3, \quad \text{for Model w/E .} \tag{8}$$

where α_1, α_2 and α_3 are dimensionless constants. These constants are determined by linearizing the dependence of λ_c on b and σ near b=10 nm and σ=1 GPa (see Figs.5b and Cb), i.e., α_1=40, α_2=$-233E_m/h_m$=−1093 and α_3=7.8 using λ_c=370 nm at b=10 nm and σ=1 GPa, that is,

$$\frac{\lambda_c}{h_m} \approx 40\left(\frac{b}{h_m}\right)-1093\left(\frac{\sigma}{E_m}\right)+7.8, \quad \text{for Model w/E ,} \tag{9}$$

which is a very convenient expression because although h_m=26 nm and E_m=122 GPa were fixed in the FEM analysis, h_m and E_m are used to normalize the dimensional variables in Eq.(9). For example, Eq.(9) predicts $\lambda_c \rightarrow 2\lambda_c$ if $h_m \rightarrow 2h_m$, $b \rightarrow 2b$ and $\Delta h_c \rightarrow 2\Delta h_c$, and Eq.(9) also predicts $\lambda_c \rightarrow \lambda_c$ if $E_m \rightarrow 2E_m$, $\sigma \rightarrow 2\sigma$ and $E \rightarrow 2E$. Since b/h_m~1 and σ/E_m~0.01 is considered (Section 2), two contributions of b/h_m and σ/E_m are found to be comparable.

The comparison of Eq.(7) for Model w/oE and Eq.(9) for Model w/E clearly shows the importance of the explicit modeling of etching process. When h_m=26 nm and E_m=122 GPa are given, Model w/oE predicts that λ_c obeys the simple scaling relation depending on h=258 nm (Eq.(7)), while Model w/E predicts that λ_c includes the dependence on b and σ (Eq.(9)).

To derive the empirical equation for the final amplitude at the final dimensions, A_f, the simple form of Eq.(8) is applied to Eq.(6) because the responses depicted in Fig.10 allow us to linearize the dependence of A_f on b and σ near b=10 nm and σ=1 GPa. Eq.(8) is approximately expressed by

$$\frac{A_\mathrm{f}}{h_\mathrm{m}} \approx \beta_1\left(\frac{b}{h_\mathrm{m}}\right)+\beta_2\left(\frac{\sigma}{E_\mathrm{m}}\right)+\beta_3, \quad \text{for Models w/oE and w/E}, \tag{10}$$

where β_1, β_2 and β_3 are dimensionless constants. These constants are determined from the gradients indicated in Fig.10. For Model w/oE, β_1=–0.71, β_2=20.68$E_\mathrm{m}/h_\mathrm{m}$=97.01 and β_3=0.805, whereas for Model w/E, β_1=0.67, β_2=0.50$E_\mathrm{m}/h_\mathrm{m}$=2.35 and β_3=0.037. Eq.(10) yields

$$\frac{A_\mathrm{f}}{h_\mathrm{m}} \approx \begin{cases} -0.71\left(\dfrac{b}{h_\mathrm{m}}\right)+97.01\left(\dfrac{\sigma}{E_\mathrm{m}}\right)+0.805, & \text{for Model w/oE} \\ 0.67\left(\dfrac{b}{h_\mathrm{m}}\right)+2.35\left(\dfrac{\sigma}{E_\mathrm{m}}\right)+0.037, & \text{for Model w/E} \end{cases}, \tag{11}$$

which provides the scaling relation showing the dependence of $A_\mathrm{f}/h_\mathrm{m}$ on b/h_m and σ/E_m since E/E_m=0.105 and h/h_m=9.923 are fixed. When b/h_m~1 and σ/E_m~0.01 is considered (Section 2), Model w/oE predicts $A_\mathrm{f}/h_\mathrm{m}$ consisting of near equal contributions of b/h_m and σ/E_m, whereas Model w/E predicts $A_\mathrm{f}/h_\mathrm{m}$ depending mainly on the contribution of b/h_m. In addition, as b/h_m decreases, Model w/oE predicts the increase in $A_\mathrm{f}/h_\mathrm{m}$, whereas Model w/E predicts the decrease in $A_\mathrm{f}/h_\mathrm{m}$.

The characteristic features elucidated here lead to the conclusion that when the etching process is explicitly introduced in etching-induced wiggling analysis (i.e., the use of Model w/E), completely opposite tendencies are predicted compared with the predictions of Model w/oE without the etching process.

5.2. Investigation of second bifurcation in postbuckling analysis

Step-by-step eigenvalue buckling analysis (Section 2.4) enables an investigate of the possibility of second bifurcation under the bifurcated path in the Abaqus analysis. The additional increase of the compressive stress in the mask layer, $\Delta\sigma_\mathrm{add}$, is used as a dummy loading parameter (Section 2). In Fig.11, $\Delta\sigma_\mathrm{add}/\sigma$ is plotted as a function of $\Delta h/h$ for b=20 nm and σ=1 GPa. The blue ▼ label represents the critical point of first bifurcation under the primary path (see Fig.5 and Fig.6b). In the postbuckling analysis, if $\Delta\sigma_\mathrm{add}/\sigma$ approaches 0 again, the corresponding point is regarded as the critical point of second bifurcation (Eqs.(2) and (3)). If $\Delta\sigma_\mathrm{add}/\sigma$ remains positive, no second

bifurcation occurs. In other words, $\Delta\sigma_{add}/\sigma$ can be regarded as a measure of the energy barrier needed to transform a different wiggling mode. Etching (i.e., the increase in $\Delta h/h$) decreases this energy barrier. When $\Delta\sigma_{add}/\sigma=0$, bifurcations occur. Fig.11 shows that the second bifurcation occurs at $\Delta h/h\approx0.9$ (red ▼ label). This point is almost identical to that at which the incremental analysis failed in the postbuckling analysis (Fig.9b). This agreement indicates that the interaction between the occurrence of second bifurcation and the explicit modeling of the etching process can cause no convergence under incremental analysis in postbuckling (Fig.9b,c).

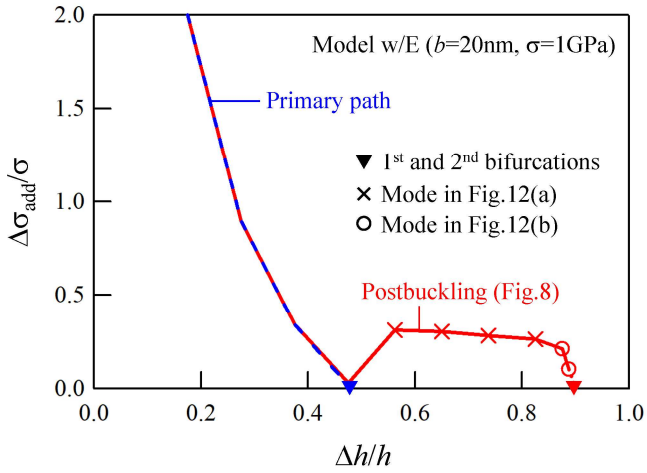

Fig.11 $\Delta\sigma_{add}/\sigma$ as a function of $\Delta h/h$, which is selected as the base state for step-by-step eigenvalue analysis under postbuckling analysis for Model w/E with b=20 nm.

Fig.12 shows the 1st buckling modes for points × and ○ in Fig.11 for the postbuckling analysis. Fig.12a may be meaningless because this buckling mode only appears when $\Delta\sigma_{add}/\sigma$ is positive. In contrast, when $\Delta\sigma_{add}/\sigma$ approaches 0, the dominant buckling mode changes to the mode observed in Fig.12b. In Fig.12, the buckling modes are superposed on the deformation states at each value of $\Delta h/h$=0.563 and 0.888 (i.e., $A\approx10-15$ nm with λ_c=769 nm). As observed in Fig.12, the amplitude of the buckling modes is sufficiently larger than the amplitude of wiggling because of the first bifurcation. Fig.12b indicates that the second bifurcation mode does not have a simple sinusoidal wave profile (cf. Fig.6b); however, the average wavelength of this non-uniform wave profile is estimated to be approximately 1000 nm (cf. 769 nm of first bifurcation). This finding indicates that the second bifurcation can occur and has the

tendency to increase the wavelength, which can be expected to contribute to further elastic energy release; however, this wavelength is shorter than that predicted by Model w/oE without the etching process (i.e., 1250 nm). A third bifurcation may also occur after the second bifurcation, especially for b=10 and 15 nm because the period after no convergence (Fig.9b) becomes relatively long. It must be interesting and challenging to study the postbuckling behavior after the second bifurcation [24,27]. In the present study, the authors did not perform further investigations after the second bifurcation and will further examine this problem in a future study.

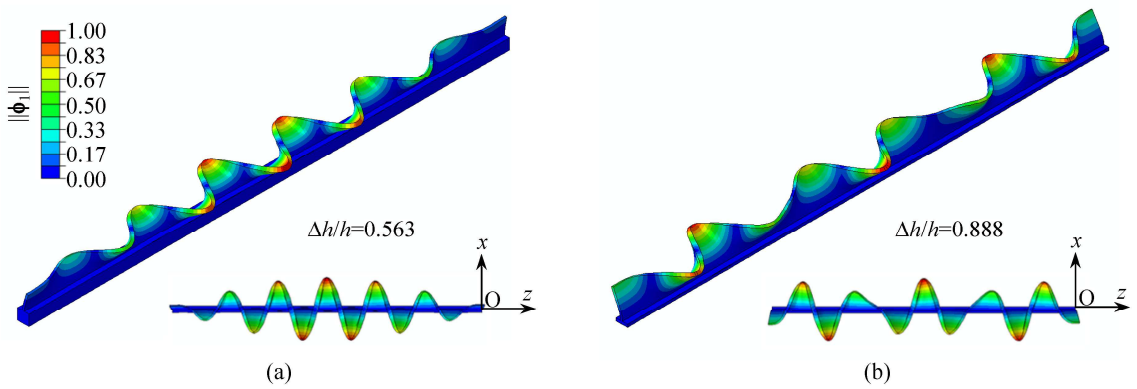

Fig.12 1st buckling mode, ϕ_1, under postbuckling analysis for Model w/E with b=20 nm: representative buckling modes at points (a) × and (b) ○ in Fig.11.

5.3. Comparison with experimental observation

The empirical equations derived in Section 5.1 are used to compare the predictions of Models w/oE and w/E with the experimental observation by Tanaka et al. [5]. Although Tanaka et al. [5] experimented with several samples of different dimensions (h=85−265 nm, h_m=24−35 nm and b=21−27 nm), the values of the observed wavelengths and final amplitudes were not measured in their paper. However, one SEM image (see the figure 2b in [5]) showed the deformation state after etching of the sample with h_m=25 nm, b=27 nm and h=265 nm (see the table 2 in [5]). In addition, E=12.8 GPa, E_m=122 GPa and σ=0.927 GPa (see the table 1 in [5]). From the SEM image, the critical wavelength, λ_c, and the final amplitude, A_f, were obtained, i.e., λ_c=600–1000 nm and A_f=10–20 nm. It is noted that it was not easy to perform a more correct measurement because the SEM image was pictured from an unknown angle.

Since h/h_m=265/25=10.600≈9.923 and E/E_m=0.105, the empirical equations derived in Section 5.1 are available. The critical wavelength is predicted using Eq.(7) for Model w/oE and Eq.(9) for Model w/E:

$$\lambda_c = \begin{cases} 1202 \text{ nm}, & \text{for Model w/oE} \\ 1067 \text{ nm}, & \text{for Model w/E} \end{cases}, \tag{12}$$

which mean that the explicit modeling of etching process decreases λ_c from 1202 nm to 1067 nm. Since Fig.9b implies that this sample does not cause second bifurcation (Section 5.2), Model w/E successfully predicts a more reasonable value of λ_c than Model w/oE (i.e., λ_c=600–1000 nm in the experiment). A small difference of Models w/oE and w/E depends on b=27 nm. As b decreases from 30 nm to 10 nm, the effect of etching process decreases λ_c dramatically (Fig.5b). Eq.(12) also implies that a further decrease in λ_c needs a different mechanism which was not considered in the FEM analysis of the present study. For example, the lateral sides of the mask–masked ridge are slightly etched during etching process [5]. If b decreases during etching process, the critical etched height decreases so that the critical wavelength can also become shorter.

Although the final amplitude is predicted using Eq.(11), it may not be appropriate to enter b=27 nm because (1) the simple form of Eq.(10) was determined to reproduce the characteristic linear response of A_f at b=10–20 nm (Fig.10a), and (2) the critical wavelength predicted by Eq.(12) was more or less longer than the range expected for experimental observation. Model w/E can provide the more reasonable value of λ_c than Model w/oE. When the use of Model w/E is focused on, the substitution of b=27 nm into Eq.(11) gives

$$A_f = 19.5 \text{ nm}, \quad \text{for Model w/E}. \tag{13}$$

Model w/E is found to predict a reasonable value of A_f (i.e., A_f=10–20 nm in the experiment). However, Fig.10a indicates that the prediction by Model w/E has the tendency to overestimate A_f at b=27 nm. To overcome this problem, a more complex form is needed instead of assuming the simple form of Eq.(10). In addition, if the critical wavelength decreases from the larger value (Eq.(12)) to 600–1000 nm in the experiment, this decrease causes a decrease in A_f (Figs.5b and 10a). Model w/E has a

potential to approach the experimental value of A_f=10–20 nm when the prediction of the critical wavelength is improved.

As mentioned in this section, if the prediction of the critical wavelength is improved, a shorter wavelength allows the amplitude to be saturated during etching process, resulting in decreasing the final amplitude. To obtain more correct empirical equations, the finite element modeling is needed to be more complicated, and the FEM analysis is needed to provide more accurate values. However, the empirical equations derived in Section 5.1 have the simple forms and show the importance of the explicit modeling of etching process. This effect appears dramatically as b decreases from 30 nm to 10 nm.

6. Concluding remarks

In the present study, etching-induced wiggling in a mask–masked layer structure was investigated using buckling and postbuckling analyses. It was assumed that the intrinsic compressive stress was included in the mask layer and that the etching process selectively removed the unmasked regions in the masked layer to create the mask–masked ridge of the final dimensions. Two mask–masked ridge models without and with the etching process (i.e., Models w/oE and w/E, respectively) were employed. Model w/E was investigated using a step-by-step eigenvalue buckling analysis. The main findings of this study are as follows.

In the explicit modeling of etching process, the wiggling behavior showed completely opposite tendencies. Model w/oE predicted a constant value of the critical wavelength of wiggling regardless of the change in ridge width, and a monotonic increase in the wiggling amplitude with the constant wavelength. In contrast, Model w/E predicted a shorter wavelength depending on the decrease in ridge width and the increase in the intrinsic compressive stress, and the saturation of the wiggling amplitude owing to the decrease in the critical wavelength. Although the maximum energy release due to buckling is achieved by a longer wavelength predicted by Model w/oE, etching-induced buckling enables the temporal dimensions during etching to cause buckling, resulting in a smaller energy release with a shorter wavelength. Thus, an additional energy release may be caused by the occurrence of second bifurcation. In

addition, the empirical equations for the critical wavelength and the final amplitude were obtained from dimensional analysis. The comparison of the empirical equations with experimental observation showed that Model w/E successfully predicts a more reasonable value of the critical wavelength than Model w/oE. Thus, the importance of the explicit modeling of etching process was confirmed. However, to obtain more correct empirical equations, the finite element modeling will be needed to be more complicated, and the FEM analysis will be needed to provide more accurate predictions. The aforementioned findings will be helpful for the development of more sophisticated fabrication process for the mask–masked ridges.

Finally, in a different point of view, the concept of step-by-step eigenvalue buckling analysis will be useful for bifurcation analysis of advanced materials, such as swollen elastomers [12,28–30], growing matter [31] and dielectric elastomers [32]. That is because when these advanced constitutive models are implemented into commercial finite element packages using user-defined material subroutines (UHYPER or UMAT in Abaqus), the external stimuli and changes inducing the characteristic deformations cannot be used as a loading parameter (Q in Eq.(2)). Bifurcation analyses for the advanced materials are definitely challengeable and should be conducted in the near future.

Acknowledgments

This research was supported by the Japan Society for the Promotion of Science (JSPS) under a Grant-in-Aid for Challenging Research (Exploratory) (No.JP17K18826). We thank Tiffany Jain, M.S., from Edanz Group (www.edanzediting.com/ac) for editing a draft of this manuscript.

Appendix A. Relation of L and λ

As described in Section 2.3, the displacements are constrained along the z-direction on the two ends of the ridges (z=0 and $-L$). This constraint allows the wavelength of wiggling to be discretized depending on the length L in the eigenvalue buckling analysis. The value of the discretized wavelengths, λ, is expressed using the relation $\lambda=2L/n$, where n is a positive integer. In the present case of L=5000 nm, eigenvalue buckling

analysis can capture the wavelengths of λ=10000, 5000, 3333, 2500, 2000, 1667, 1429, 1250, 1111, 1000, 909, 833, 769, 714,… nm as individual buckling modes. This resolution is sufficient to compare with the experimentally observed wavelength smaller than 1000 nm (Section 5.3).

Appendix B. Introduction of $\Delta\sigma$ and Δh

The compressive stress in the mask layer, $\Delta\sigma$, and the etching height, Δh, are introduced into the Abaqus analysis. First, the displacements are constrained along the z-direction on the two ends of the ridges such that the compressive stress, $\Delta\sigma$, in the direction is generated using the isotropic thermal expansion, i.e., $\Delta\sigma=\alpha E_m \Delta T$, where α is the thermal expansion coefficient and ΔT is the incremental temperature. The individual values of α and ΔT have no meaning in the analysis, and α is adjusted to scale ΔT=1000 K to $\Delta\sigma$=1000 MPa (=1 GPa). Next, a dimensionless field valuable, S, is introduced to control the etching height, Δh, in the analysis of Model w/E, and to scale ΔS=80 to $\Delta h=h$ (=258 nm in the present study) because the unmasked layer supposed to be etched is equally divided into 80 layers in the y-direction (Section 2.3). The increase in ΔS from 0 to 80 is used as the loading parameter to reproduce the etching from the top face (Δh =0) to the bottom face ($\Delta h=h$). The thickness of one layer is approximately 3.2 nm (=258 nm/80 layers).

Appendix C. Effect of σ on Δh_c and λ_c

Fig.C shows the effects of σ on the critical buckling point predicted in Model w/E. To this end, the ridge width is fixed at b=10 nm. In the postbuckling analysis (Fig.9c), the 1st buckling modes for individual values of σ were used as imperfections. The difference between the FVK and FEM approaches is almost undetectable in Fig.C because of the small value of b=10 nm (see Fig.4) regardless of the change of σ, as a thin plate is assumed in the FVK plate theory [5].

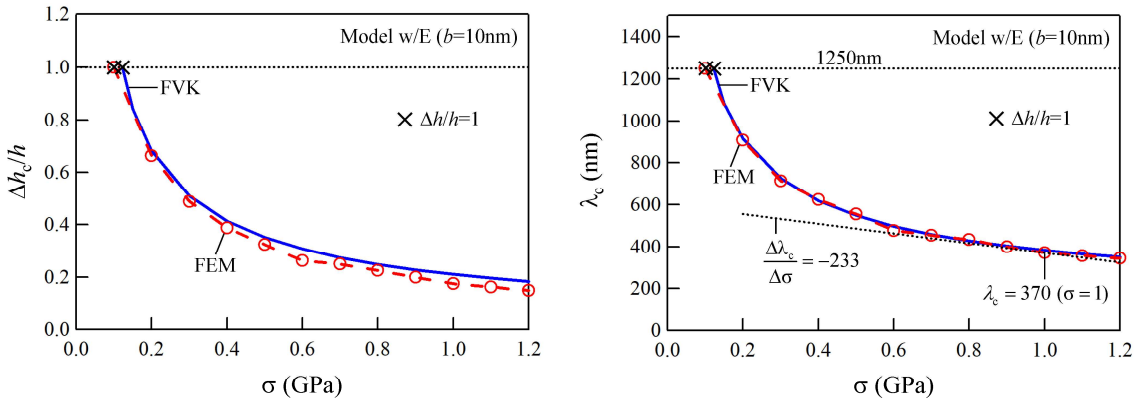

Fig.C Effect of σ on the critical buckling point predicted in Model w/E: (a) critical etching depth, $\Delta h_c/h$, and (b) critical wavelength, λ_c.

References

[1] Darnon M, Chevolleau T, Joubert O, Maitrejean S, Barbe JC, Torres J. Undulation of sub- 100 nm porous dielectric structures: A mechanical analysis. Appl Phys Lett 2007;91:194103.

[2] Darnon M, Chevolleau T, David T, Ducote J, Posseme N, Bouyssou R, Bailly F, Perret D, Joubert O. Patterning of porous SiOCH using an organic mask: Comparison with a metallic masking strategy. J Vac Sci Tech B 2010;28:149–56.

[3] Eugène L, Gour MJ. Unexpected undulations produced from deformed nanowires. Materials Today 2011;14:503.

[4] Baklanov MR, de Marneffe JF, Shamiryan D, Urbanowicz AM, Shi H, Rakhimova TV, Huang H, Ho PS. Plasma processing of low-k dielectrics. J Appl Phys 2013;113:041101.

[5] Tanaka H, Hidaka T, Izumi S, Sakai S. Onset of wiggling in a microscopic patterned structure induced by intrinsic stress during the dry etching process. J Appl Mech 2014;81:091009.

[6] Kim J, Chae YS, Lee WS, Shon JW, Kang CJ, Han WS, Moon JT. Sub-0.1 μm nitride hard mask open process without precuring the ArF photoresist. J Vac Sci Tech B 2003;21:790–4.

[7] Mora T, Boudaoud A. Buckling of swelling gels. Euro Phys J E 2006;20:119–24.

[8] DuPont Jr SJ, Cates RS, Stroot PG, Toomey R. Swelling-induced instabilities in microscale, surface-confined poly(N-isopropylacryamide) hydrogels. Soft Matter 2010;16:3876–82.

[9] Kang MK, Huang R, Swelling-induced instability of substrate-attached hydrogel lines. Int J Appl Mech 2011;3:219–33.

[10] Kang SH, Shan S, Noorduin WL, Khan M, Aizenberg J, Bertoldi K. Buckling-Induced Reversible Symmetry Breaking and Amplification of Chirality Using Supported Cellular Structures. Adv Mater 2013;25:3380–5.

[11] Zhao Y, Shao ZC, Li GY, Zheng Y, Zhang WY, Li B, Cao Y, Feng XQ. Edge wrinkling of a soft ridge with gradient thickness. Appl Phys Lett 2017;110: 231604.

[12] Hong W, Liu ZS, Suo Z. Inhomogeneous swelling of a gel in equilibrium with a solvent and mechanical load. Int J Solids Struct 2009;46:3282–9.

[13] Kang MK, Huang R. A variational approach and finite element implementation for swelling of polymeric hydrogels under geometric constraints. J Appl Mech 2010;77:061004.

[14] Okumura D, Kuwayama T, Ohno N. Effect of geometrical imperfections on swelling-induced buckling patterns in gel films with a square lattice of holes. Int J Solids Struct 2014;51:154–63.

[15] Okumura D, Inagaki T, Ohno N. Effect of prestrains on swelling-induced buckling patterns in gel films with a square lattice of holes. Int J Solids Struct 2015;58:288–300.

[16] Okumura D, Sasaki A, Ohno N. Swelling-induced buckling patterns in gel films with a square lattice of holes subjected to in-plane uniaxial and biaxial pretensions. Adv Struct Mater 2015;64:319–34.

[17] Toh W, Ding Z, Ng TY, Liu ZS. Wrinkling of a polymeric gel during transient swelling. J Appl Mech 2015;82:061004.

[18] Abaqus 6.14 User Documentation, 2014, Dassault Systems SIMULIA Corporation.

[19] Bower AF. Applied Mechanics of Solids, 2010, CRC Press, Taylor & Francis Group.

[20] Sugiura J, Okumura D, Tanaka H. Comparative analysis of out-of-plane undulation buckling in microscopic patterned structure. Trans Japan Soc Comp Meth Eng 2016;16:53–8 (in Japanese).

[21] Bertoldi K, Boyce MC, Deschanel S, Prange SM, Mullin T. Mechanics of deformation-triggered pattern transfromations and superelastic behavior in periodic elastomeric structures. J Mech Phys Solids 2008;56:2642–68.

[22] Hill R. A general theory of uniqueness and stability in elastic–plastic solids. J Mech Phys Solids 1958;6:236–49.

[23] Ohno N, Okumura D, Niikawa T. Long-wave buckling of elastic square honeycombs subject to in-plane biaxial compression. Int J Mech Sci 2004;46:1697–713.

[24] Okumura D, Ohno N, Noguchi H. Elastoplastic microscopic bifurcation and post-bifurcation behavior of periodic cellular solids. J Mech Phys Solids 2004;52:641–66.

[25] Okumura D, Kasugai A. Eigenvalue buckling analysis of swelling-induced pattern transformation in porous gel films. Trans Japan Soc Comp Eng Sci 2016;2016:20160020 (in Japanese).

[26] Jawed MK, Da F, Joo J, Grinspun E, Reis PM. Coiling of elastic rods on rigid substrates. PNAS 2014;111:14663–8.

[27] Combescure C, Henry P, Elliott RS. Post-bifurcation and stability of a finitely strained hexagonal honeycomb subjected to equi-biaxial in-plane loading. Int J Solids Struct 2016;88–89:296–318.

[28] Chester SA, Anand L, A coupled theory of fluid permeation and large deformations for elastomeric materials. J Mech Phys Solids 2010;58:1879–906.

[29] Okumura D, Kondo A, Ohno N. Using two scaling exponents to describe the mechanical properties of swollen elastomers. J Mech Phys Solids 2016;90:61–76.

[30] Okumura D, Mizutani M, Tanaka H, Uchida M. Effects of two scaling exponents on biaxial deformation and mass transport of swollen elastomers. Int J Mech Sci (inprint).

[31] Kuhl E. Growing matter: A review of growth in living systems. J Mech Behavior Biomed Mater 2014;29:529–43.

[32] Henann DL, Chester SA, Bertoldi K. Modeling of dielectric elastomers: Design of actuators and energy harvesting devices. J Mech Phys Solids 2013;61:2047–66.